A Case Study of Convective Boundary Layer Development during IHOP_2002: Numerical Simulations Compared to Observations

ROBERT J. CONZEMIUS

School of Meteorology, University of Oklahoma, Norman, Oklahoma, and Windlogics, Inc., Grand Rapids, Minnesota

EVGENI FEDOROVICH

School of Meteorology, University of Oklahoma, Norman, Oklahoma

(Manuscript received 8 March 2007, in final form 4 November 2007)

ABSTRACT

Results are presented from a combined numerical and observational study of the convective boundary layer (CBL) diurnal evolution on a day of the International H_2O Project (IHOP_2002) experiment that was marked by the passage of a dryline across part of the Oklahoma and Texas Panhandles. The initial numerical setup was based on observational data obtained from IHOP_2002 measurement platforms and supplementary datasets from surrounding locations. The initial goals of the study were as follows: (i) numerical investigation of the structure and evolution of the relatively shallow and homogeneous CBL east of the dryline by means of large-eddy simulation (LES), (ii) evaluation of LES predictions of the sheared CBL growth against lidar observations of the CBL depth evolution, and (iii) comparison of the simulated turbulence structures with those observed by lidar and vertically pointing radar during the CBL evolution. In the process of meeting these goals, complications associated with comparisons between LES predictions and atmospheric observations of sheared CBLs were encountered, adding an additional purpose to this study, namely, to convey and analyze these issues.

For a period during mid- to late morning, the simulated CBL evolution was found to be in fair agreement with atmospheric lidar and radar observations, and the simulated entrainment dynamics were consistent with those from previous studies. However, CBL depths, determined from lidar data, increased at a faster rate than in the simulations during the afternoon, and the wind direction veered in the simulations more than in the observations. The CBL depth discrepancy can be explained by a dryline solenoidal circulation reported in other studies of the 22 May 2002 case. The discrepancy in winds can be explained by time variation of the large-scale pressure gradient, which was not included in LES.

1. Introduction

This paper summarizes results from a research effort to numerically simulate the structure and evolution of a dry (or clear; see Holtslag and Duynkerke 1998) convective boundary layer (CBL) during the 22 May 2002 observations taken as a part of the International H_2O Project (IHOP_2002) experiment (Weckwerth et al. 2004)—a day on which the wind shear was relatively strong. In a traditional sense, the dynamics of such a CBL are primarily driven by a positive buoyancy source at the underlying surface. However, a purely buoyancy-driven CBL rarely exists. In some situations, the presence of wind shear may significantly modify the CBL dynamics, especially with respect to the convective entrainment, which is the principal mechanism of the CBL growth (Conzemius and Fedorovich 2006a).

A vast dataset of observations was available from the IHOP_2002 experiment for this particular case, which, given its strong winds, presented some of the best conditions during IHOP_2002 for comparing the observed evolution of the sheared atmospheric CBL with large-eddy simulation (LES; Moeng and Sullivan 1994; Pino et al. 2003; Conzemius and Fedorovich 2006a). The primary goals of the study are twofold. First, we intend to evaluate LES predictions of the sheared CBL growth against lidar observations of CBL depth evolution and compare LES output with radiometer, radar, and radiosonde data to more fully understand the evolution of

Corresponding author address: Robert J. Conzemius, Windlogics, Inc., 201 NW 4th St., Grand Rapids, MN 55744.
E-mail: robert.conzemius@att.net

DOI: 10.1175/2007MWR2193.1

the mean wind and temperature in the CBL, thereby allowing us to place the results of the earlier study of Conzemius and Fedorovich (2006a) within the context of atmospheric CBL observations.

Although the presented case was an intensive observation period (IOP) for studying convection initiation along the dryline, the simulation focused on the more homogeneous CBL east of the dryline. Even so, simulating the evolution of the more homogeneous CBL on its own presented some important challenges. Thus, the second major goal of the presented study is to convey and analyze the difficulties encountered when making comparisons between LES predictions and atmospheric observations of sheared CBLs, particularly for the 22 May 2002 case. While LES typically involves idealized flows, Lothon et al. (2006) have studied a CBL case by comparing simulations and observations. Despite its limitations, LES shows promise for simulating real cases, and it will likely have important applications in the future (in particular, to the wind energy industry) because of its ability to resolve nonsteady turbulent flows. Thus, identifying the successes and drawbacks of LES for actual atmospheric cases is essential for its application.

Additionally, one hope for studying this particular case was to expand on previous dryline modeling studies (Ziegler et al. 1997; Peckham et al. 2004; Xue and Martin 2006a,b) by performing a high-resolution LES of the dryline and comparing the LES output with fine-scale radar observations (Weiss et al. 2006, 2007). Although the technical requirements of prescribing lateral boundary conditions for heterogeneous CBLs of this type made these goals too ambitious for the available computer power and LES numerical code, we hope to lay some groundwork and present some considerations for simulating heterogeneous CBLs of this type in the future. With this overall goal in mind, we aimed to adequately simulate the structure of the relatively shallow and homogeneous CBL east of the dryline, hoping to reproduce CBL turbulence patterns that are at least qualitatively comparable with the patterns that are observed in the atmosphere east of the dryline.

2. Observational input data and numerical setup

The studied case was the 22 May 2002 convection initiation experiment that took place over the Oklahoma and Texas Panhandles. Numerous CBL measurements were taken on that day using a variety of mobile and fixed ground-based instruments as well as lidar- and radar-equipped aircraft. The target of the measurements was a north–south-oriented dryline that moved slowly eastward across the panhandles.

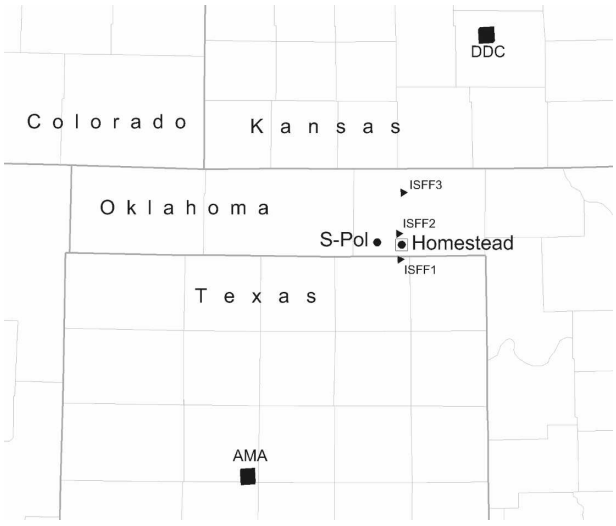

FIG. 1. Locations of LES grid and observational data input to LES. Large squares indicate the position of NWS radiosonde observations, triangles denote the locations of ISFF sites, and the S-Pol and Homestead locations are marked by circles. The small square surrounding the Homestead location indicates the size of the LES grid.

a. Observational input data

During IHOP_2002, intensive profiler, radiosonde, and lidar measurements were taken at a field station about 30 km southwest of Beaver, Oklahoma, which was designated, for operational coordination purposes, as the Homestead site. A 10-cm research radar [S-band dual-polarization Doppler radar (S-Pol); Weckwerth et al. 2004] was located approximately 17 km west of this site. Three integrated surface flux facility (ISFF) stations were deployed in the Oklahoma and Texas Panhandles along an approximately 50-km north–south line centered on the Homestead site. Additionally, balloon-borne sounding data were available from nearby National Weather Service (NWS) launch sites at Amarillo, Texas (AMA), and Dodge City, Kansas (DDC). Figure 1 shows the locations of these measurement sites. The overall IHOP_2002 field measurement layout is described in greater detail in Weckwerth et al. (2004).

The observational data used for the simulation input consisted of radiosonde data from AMA and DDC, data from the Atmospheric Emitted Radiance Interferometer (AERI) mounted on a 1994 Winnebago (AERIBAGO; Feltz et al. 2003), which was located at the Homestead site, and surface flux measurements from the three ISFF stations. For comparison with LES output, CBL depth estimates were available from lidars located at the Homestead site.

The initial wind profile data were taken from a combination of the AMA and DDC soundings. Because the

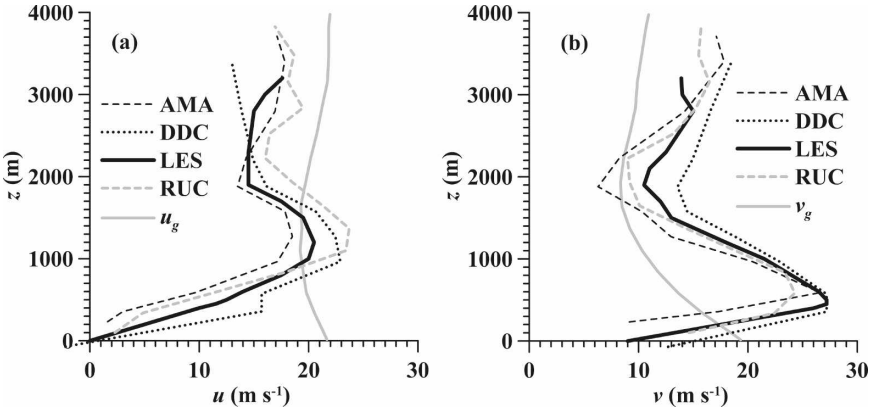

FIG. 2. Wind profiles for the 1200 UTC 22 May 2002 case: (a) x component (u) and (b) y component (v). The solid black profile indicates the initial LES wind, the solid gray profile is the initial geostrophic wind taken from the nearest RUC analysis grid point, the dashed gray profile is the RUC analyzed wind, the dashed black profile is from the AMA 1200 UTC sounding, and the black dotted profile is from the DDC 1200 UTC sounding.

Homestead site is about midway between AMA and DDC, the wind data were interpolated in a linear fashion between the two soundings. Additionally, to calculate geostrophic wind vectors, the large-scale pressure gradient was retrieved from Rapid Update Cycle (RUC) hourly pressure-level analyses, which in turn were retrieved from the National Centers for Environmental Prediction (NCEP). The geostrophic wind vectors at 1200, 1500, 1800, and 2100 UTC 22 May and 0000 UTC 23 May were averaged to produce the vertical profile of geostrophic wind vectors that was used throughout the run. The geostrophic wind was taken to be constant in time during the simulation. With the exception of the last 2 h of the simulation, the RUC data showed that the geopotential height gradients changed relatively little during the day on 22 May 2002, so this seems to be a reasonable assumption.

The profiles of initial wind and geostrophic wind used in the simulation are shown in Fig. 2, together with wind data from the AMA and DDC soundings. The initial profiles indicate wind speeds of up to 30 m s^{-1}, and although the geostrophic wind shear was not particularly strong, the shear in the measured wind was even stronger than in the sheared CBL case simulated in Conzemius and Fedorovich (2006a), which was considered to be at the upper limit of a realistic range for atmospheric shear magnitudes for CBL conditions. The x component alone changes by 20 m s^{-1} over the lowest kilometer, and the overall wind speed also changes by 20 m s^{-1} in less than 1 km. Note that in this particular case, unlike in Conzemius and Fedorovich (2006a), most of the shear was contained in the ageostrophic component of the wind.

The initial LES virtual potential temperature profile was taken from AERIBAGO temperature and water vapor data. The AERI data were compared with AMA and DDC 1200 UTC soundings (see Fig. 3) and found to be reasonably consistent with those data over most

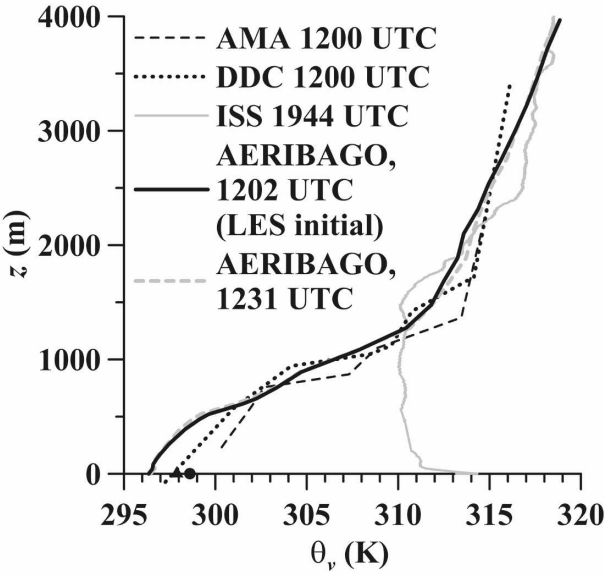

FIG. 3. Virtual potential temperature profiles for the 22 May 2002 CBL case. The solid black profile indicates the AERIBAGO 1202 UTC sounding (same as the initial LES profile), the dashed gray profile is the AERIBAGO 1231 UTC sounding, the black dashed profile is from the Amarillo 1200 UTC sounding, and the black dotted profile is from the Dodge City 1200 UTC sounding. The solid gray profile is from the ISS 1944 UTC sounding and is plotted to illustrate the change in the actual temperature profile over the course of the simulation. The black triangle indicates the 3-m virtual potential temperature at the ISFF2 flux site (see Fig. 1). The black circle is the ISS virtual potential temperature at the Homestead site.

of the 4-km depth of the LES domain, except for the lowest few hundred meters. Surface observations taken from the Homestead site and ISFF2 (see Fig. 1) indicated that the AMA and DDC soundings were likely more representative of the low-level virtual potential temperature at the Homestead site than were the AERI data. The data indicate that the virtual potential temperature gradient is roughly 0.010 K m^{-1} in the lowest kilometer, which corresponds to the strongest stratification reproduced in the sheared CBL simulations of Conzemius and Fedorovich (2006a).

Surface heat flux data are presented in Fig. 4. We considered the technique presented in Angevine et al. (1998) to integrate the surface fluxes across all three stations, but because the fluxes varied very little among the stations and the surrounding area was relatively homogeneous semiarid grassland, a simple average was taken for input to LES. Half-hourly averages of sensible heat flux from all three ISFF measurement stations were averaged to produce the LES input flux data. The flux data are indicative of the strong insolation and absence of cloud cover that occurred during this particular case.

The atmospheric CBL depths were determined from the Holographic Airborne Rotating Lidar Instrument Experiment (HARLIE; Guerra et al. 1999) data. HARLIE is a 1-μm-wavelength aerosol backscatter lidar that was deployed during IHOP_2002 at the Homestead site south-southwest of Beaver. HARLIE makes atmospheric scans at a constant elevation angle of 45° and rotates continuously in azimuth at a rate of 30° s^{-1}, thus providing five scans per minute. The five scans form a 1-min average that is used to diagnose the CBL depth.

The HARLIE scanning strategy covers a somewhat smaller area (at the CBL top) than the horizontally averaged area in LES. If the CBL depth is 2 km, the scan sweeps a circle whose radius is 2 km. The area circumscribed by this circle is 12.5 km. During the scanning period, the CBL structures move with the flow, so if the flow is 15 m s^{-1} or greater (as in this case), the structures will move approximately 1 km or more during the scanning process, thereby adding about 4 km to the swept area. The resulting total area inside the swept circles is therefore roughly 16 km^2. By comparison, the LES domain horizontal area is 59 km^2. One might expect that the HARLIE statistics, with a smaller horizontal sample area, would converge less to what might be considered in this case to be an ensemble mean; therefore, more variation in the CBL depth estimates would be expected from HARLIE data than from LES. As the CBL depth increases and the CBL mean flow increases, the HARLIE-sampled area at the CBL top becomes greater.

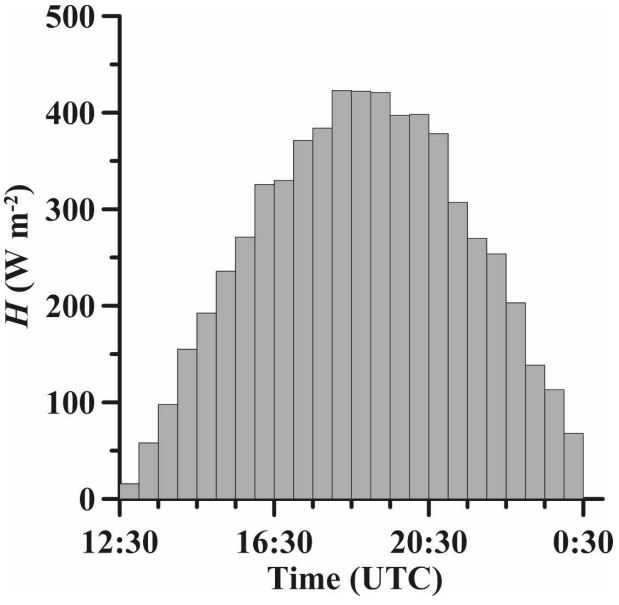

FIG. 4. Surface sensible heat flux (W m^{-2}) as a function of time in the simulation of the 22 May 2002 CBL case obtained from ISFF data.

The CBL depth was determined from the lidar data using a Haar wavelet transform as described in Davis et al. (2000). The transform was applied to the 1-min-averaged vertical profiles of lidar backscatter (five scans). For comparison, the same wavelet technique was also applied to the LES potential temperature profiles. A wavelet dilation of 10 was used, which corresponds approximately to 300 m at the LES vertical resolution of 30 m. The CBL depth estimations from the buoyancy flux minimum technique, commonly used in LES, will also be shown later for comparison. Although the wavelet transforms are applied to profiles of different scalars (potential temperature versus aerosol backscatter), the Haar wavelet transform used in this technique reaches its maximum in layers with large gradients, which should be essentially the same for aerosols and potential temperature in the CBL, provided the entrainment zone interface is sharp. Because it responds to large vertical gradients of CBL scalars, the wavelet technique provides CBL depth estimates that are consistent with those from the maximum temperature gradient technique that is discussed in Sullivan et al. (1998) and Fedorovich et al. (2004c).

b. Numerical setup

The LES code employed in the present study is a further modification of the code described in Nieuwstadt and Brost (1986) and Fedorovich et al. (2001, 2004a,c). The code was extensively tested in compari-

TABLE 1. Parameters of conducted LES.

Parameter	Setting
Domain size	$7.68 \times 7.68 \times 3.99$ km^3
Grid	$256 \times 256 \times 133$ (30-m cells)
Starting time	1230 UTC
Time step	Evaluated from a numerical stability constraint
Time advancement	Leapfrog scheme with weak Asselin filter
Representation of advection and diffusion terms	Centered second-order finite-difference approximations
Lateral boundary conditions	Periodic for all prognostic variables and pressure
Upper boundary conditions	Neumann with zero gradient for velocity components; a sponge layer imposed in the upper 20% of simulation domain
Lower boundary conditions	No slip for velocity; Neumann for temperature, pressure, and subgrid TKE; Monin–Obukhov similarity functions as in Fedorovich et al. (2001)
Subgrid turbulence closure	Subgrid TKE based on Deardorff (1980)
Grid frame of reference	$u = 14$ m s^{-1}; $v = 10$ m s^{-1}

son against several other representative LES codes, experimental data, and bulk model predictions for clear CBLs with and without wind shear (Fedorovich et al. 2001, 2004a,c; Conzemius and Fedorovich 2006a,b, 2007), and it was found capable to adequately reproduce the main features of turbulent flow regimes in a broad variety of clear CBL conditions.

The LES settings are listed in Table 1. The grid cell dimensions were set to be 30 m in both horizontal and vertical dimensions in order to provide a domain that was sufficiently deep (4 km) to capture the CBL growth during the day and sufficiently wide (7.68 km) to reproduce the horizontal convective rolls while still meeting the constraints of computer memory. During the latter stages of the CBL development, the CBL depth and horizontal convective roll crosswise dimension were sufficiently large that the LES domain and the associated periodic boundary conditions could constrict their development somewhat. However, the simulated CBL did not grow as deep as in the observations (see section 3).

To minimize numerical damping of large wavenumber turbulence and to maximize the time step (Conzemius 2004), a moving-grid frame of reference was used in the conducted LES runs. The particular values of the frame-of-reference velocity components, relative to ground, were chosen according to the prescribed profiles of geostrophic wind in LES (see Table 1 and section 2a), and these values were held constant in both horizontal directions.

To provide a more realistic initialization of turbulence and development of CBL conditions as the surface heat flux transitioned from negative to positive, the LES was prerun for 2 h with a weak negative heat flux at the lower surface in order to develop coherent turbulent structures representative of those occurring just after sunrise. The turbulent components of the flow in this presimulation stage were then saved and added to the initial mean profiles (see Figs. 2 and 3) to provide the initial conditions for the simulation.

Turbulence statistics were calculated every 100 time steps during the simulation, and cross sections of virtual potential temperature and velocity components were produced every 1000 time steps. These cross sections were taken from the y–z and x–z planes in the interior of the grid as well as from an x–y plane at the lowest aboveground model grid level.

3. Results

a. Evolution of entrainment

The shear in the considered CBL case appears to have a rather substantial effect on entrainment. At the initial stages of the simulation, the entrainment flux ratio, which is the negative of the ratio of the entrainment heat–buoyancy flux to the surface heat–buoyancy flux, becomes extremely large (see Fig. 5a), reaching a peak value that is much larger than was seen in any of the sheared CBL simulations described in Conzemius and Fedorovich (2006a). However, the surface heat flux is only about 16 W m^{-2}, so if any entrainment zone shear is present, it will undoubtedly make a proportionally large contribution to entrainment. After this initial burst of entrainment, the entrainment flux ratio rapidly decreases to 1 and then slowly decreases to a value of approximately 0.5 by 1530 UTC. Between 1530 and 1830 UTC, it gradually diminishes to a value near 0.2, which is typical of the CBL without wind shear (Stull 1973; Fedorovich et al. 2004a; see Fig. 5b). Toward the end of the simulation, it increases to near 0.5 again.

The strong variation in entrainment flux ratios shows that the CBL is far from the equilibrium regime of

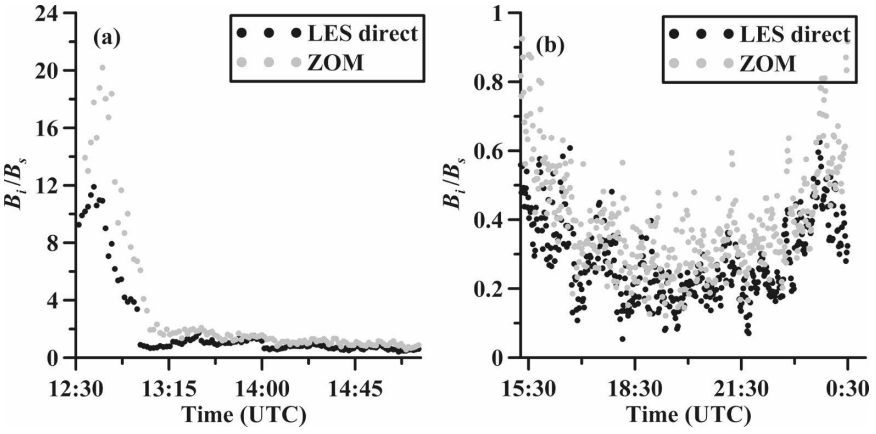

FIG. 5. Entrainment flux ratio as a function of time for the 22 May 2002 CBL case with the entrainment zone heat flux taken directly from LES (black dots) and linearly extrapolated through the zero crossing height to find the zero-order bulk model (ZOM) heat flux of entrainment (gray dots). The y axes are scaled differently (a) for the initial period of the simulation and (b) during the rest of the day in order to highlight the differences in the evolution of the entrainment flux ratio.

entrainment discussed in Fedorovich et al. (2004a) and Conzemius and Fedorovich (2006a). This is no surprise given the variability of all of the external parameters that are normally held constant in simulations of idealized CBL cases. The free atmospheric stratification is heterogeneous, requiring the CBL to adjust to the changing stratification (as discussed in Fedorovich et al. 2004b), and the surface buoyancy flux also changes, requiring some additional adjustment. As the CBL grows, it also encounters layers of different shears. All these factors strongly obstruct the establishment of an equilibrium regime during much of the simulation.

To take a closer look at the details of the CBL dynamics related to the evolution of the entrainment flux ratio during the simulation, we examine profiles of CBL statistics taken 3 times during the simulation. The first is at 1252 UTC, when the boundary layer is undergoing transition from a nocturnal planetary boundary layer (PBL) to a sheared CBL. The second is at 1944 UTC, when the entrainment flux ratio decreases to about 0.2 and the CBL evolution is governed primarily by shear-free dynamics. Additionally, Homestead Integrated Sounding System (ISS) radiosonde data are available at this time for comparison. The final time is 0000 UTC (23 May), when the entrainment flux ratio has again increased, and shear appears to be making a relatively strong contribution to CBL dynamics once again.

b. Evolution of mean profiles

The simulated virtual potential temperature profiles at these selected times are plotted in Fig. 6, and the corresponding momentum profiles are shown in Fig. 7. The upper and lower limits of the entrainment zone (which is defined as the layer of negative buoyancy flux) and the CBL top z_i are also presented in these

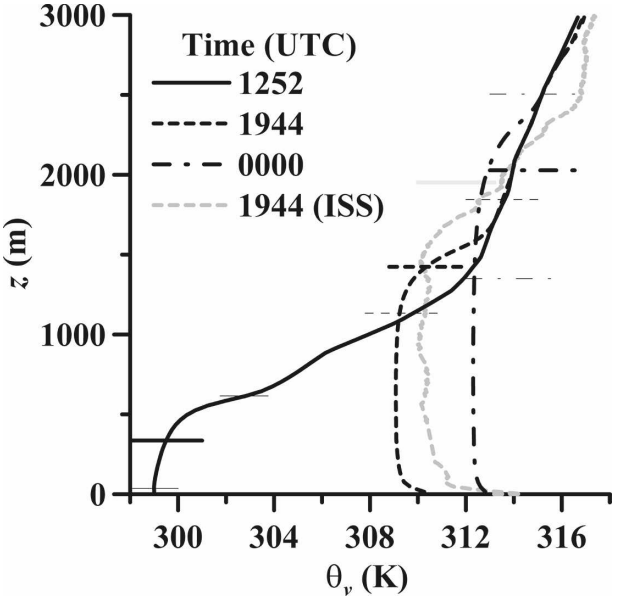

FIG. 6. Mean potential temperature profiles during the simulation of the 22 May 2002 CBL case at 1252 (solid line), 1944 (dashed line), and 0000 UTC (dashed–dotted line). The upper and lower limits of the entrainment zone are marked on each profile by thin horizontal lines, and the inversion height z_i (identified as the level of maximum entrainment flux within the entrainment zone, retrieved from the buoyancy flux profiles) is shown by bold horizontal lines. The light gray line is the ISS 1944 UTC sounding with the CBL top z_i determined by wavelet transform of the lidar backscatter profile.

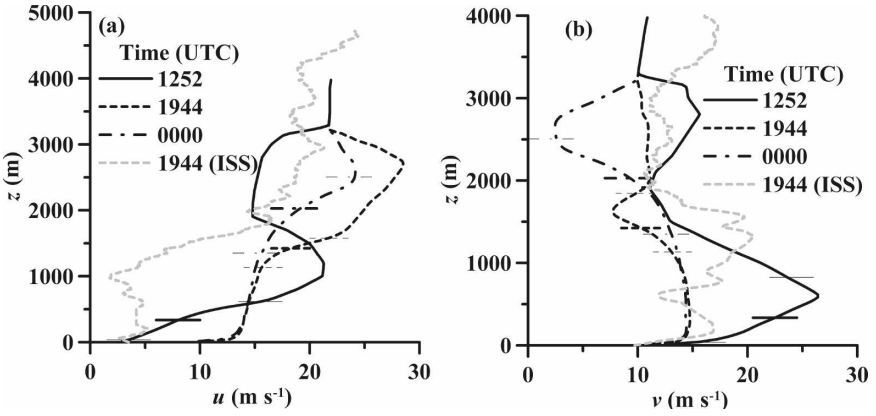

FIG. 7. Profiles of mean wind components at selected times during the simulation of the 22 May 2002 CBL case. For notation, see Fig. 6.

plots. Also plotted for comparison in Figs. 6 and 7 is the 1944 UTC ISS sounding, which will be discussed with regard to the evolution of the CBL depth (see section 3d).

At 1252 UTC (Fig. 6a), the nocturnal PBL is transitioning to a CBL, and the entrainment zone encompasses most of the PBL depth because of the strong shear production of turbulence and its dominance over the buoyancy production of TKE. There is an approximately 15 m s^{-1} velocity increment across the entrainment zone at this time. The present case is consistent with the transition discussed in Angevine et al. (2001) because of the large contribution from shear to the TKE balance, but in our case the shear contribution is particularly strong.

At 1944 UTC (Figs. 6b and 7b), the CBL is still growing underneath a rather strong inversion, but the entrainment zone shear has diminished substantially. The layer of very high momentum, seen below $z = 1500$ m at 1252 UTC, has largely disappeared because of a combination of the entrainment of this momentum into the growing CBL and the effects of the Coriolis and large-scale pressure gradient forces (accelerations resulting from the deviation of the wind from geostrophic balance). The entrainment zone, rather than growing as it typically would under conditions of uniform stratification and shear (see Figs. 10 and 11 of Conzemius and Fedorovich 2006a), has not deepened during this time period. By 0000 UTC on 23 May 2002 (Figs. 6c and 7c), both the CBL and the entrainment zone have become much deeper, influenced by a combination of the weaker stratification aloft and the increasing shear at the CBL top (13 m s^{-1} compared to 7 m s^{-1} at 1944 UTC).

It is apparent from Fig. 7 that the simulated and observed winds at 1944 UTC are substantially different. Because the pressure gradient changes relatively little during the day of 22 May 2002, the prescription of a constant (in time) geostrophic wind in the LES was assumed to be sufficient. However, the veering of the low-level winds in LES, manifested by an approximately 10 m s^{-1} difference between the simulated and observed x component (u) wind at 1944 UTC, is much stronger than it is in the ISS sounding. This points to the insufficiency of the above assumption in the considered case. The observed discrepancies will be further addressed in section 3g.

c. Turbulence kinetic energy budgets

At 1252 UTC (Fig. 8a), the shear production of turbulence dominates all the other terms in the TKE budget. Because the PBL is in transition, the entrainment zone appears to be a continuation of the nocturnal PBL rather than part of the CBL. The CBL development can only be noted from the very shallow layer of positive buoyancy flux that has developed near the surface. Certainly, the surface buoyancy flux at this time in the simulation is quite weak (see Fig. 4), so it is easy for the relative effects of shear to be rather large. The shear production of TKE throughout this entrainment zone (which could, for practical purposes, be referred to as a residual nocturnal PBL) is about 20 times the buoyancy production of TKE at the surface. The shear production seems to be mostly balanced locally by dissipation and buoyancy flux; the transport profile does not differ significantly from zero, and the residual, although positive, may be associated with a locally (in time) unbalanced production of TKE caused by the intermittency of stably stratified turbulence. In terms of shear production, there is little indication of any separation between the entrainment zone and surface layer (see also Moeng and Sullivan 1994).

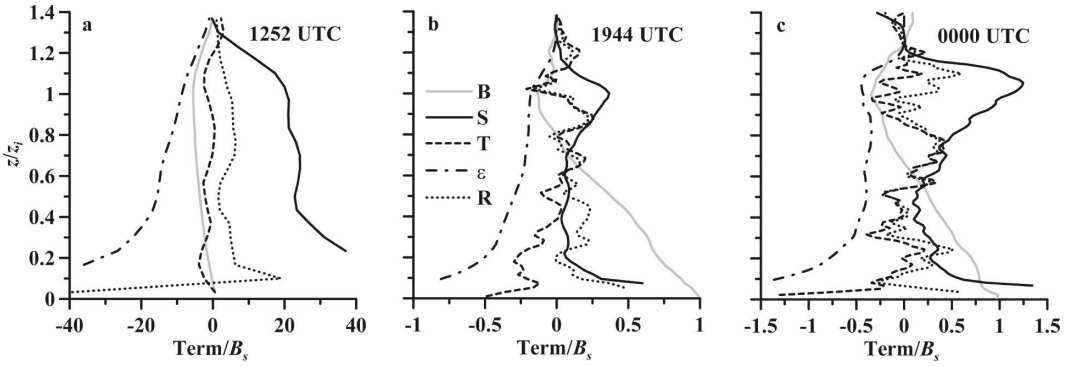

FIG. 8. Simulated TKE budgets during the simulation at (a) 1252, (b) 1944, and (c) 0000 UTC. The line styles correspond to the individual terms in the TKE budget: the solid black lines denote the shear production terms, solid gray lines the buoyancy terms, dashed black lines the vertical transport term, dotted–dashed black lines the dissipation, and dotted black lines the residual.

By 1944 UTC (see Fig. 7b), the shear production of turbulence in the entrainment zone has become much smaller. This is due to the weakening of the entrainment zone shear and the increase of the surface buoyancy flux, both of which act to diminish the relative effect of shear on entrainment. Despite this large surface flux, the strong inversion keeps the CBL growth at a very low rate, and this decreases the contribution of momentum entrainment to the shear production of TKE. The entrainment zone is relatively shallow at this time, which is characteristic of CBLs growing against strong stratification, yet it is relatively deep when compared to shear-free CBL simulations with the same amount of stratification (Conzemius and Fedorovich 2006a; Moeng and Sullivan 1994). Because of the noted features, the CBL appears to approach an equilibrium regime as the buoyancy production of turbulence in the CBL is nearly balanced by dissipation and the negative buoyancy flux of entrainment. The transport profile bears some resemblance to the typical shear-free CBL transport profile (Conzemius and Fedorovich 2006a) in that it is strongly negative near the surface and increases to zero at the base of the entrainment zone.

The very large shear production and dissipation terms in the surface layer have been truncated in Fig. 8 to highlight their TKE dynamics in the entrainment zone. Although the shear production and dissipation in the surface layer are both very strong, they are of opposite sign and therefore largely balance each other. Lenschow (1970, 1974) and Moeng and Sullivan (1994) have also shown that the shear production of TKE in the surface layer is mostly balanced by dissipation, and an analysis of a larger set of simulated CBL cases (Conzemius and Fedorovich 2006a) has shown that surface layer shear-produced TKE is not generally available for entrainment. It must be noted that the large and fluctuating residual term near the surface is probably a numerical artifact.

Near the end of the simulation (0000 UTC; see Fig. 8c), the entrainment zone shear production of TKE once again becomes about as strong as the buoyancy production at the surface. As the growing CBL encounters a layer of much weaker stratification, the entrainment zone becomes deeper, but its depth may be influenced also by increasing shear. Once again, it should be noted that the relative effects of shear appear large because the surface buoyancy flux has weakened considerably from its maximum value that occurred in the middle of the simulation. Unlike Fig. 8b, the transport profile no longer mirrors the buoyancy flux profile below the entrainment zone.

d. Profiles of Richardson numbers

Because one of the major conclusions of Conzemius and Fedorovich (2006a) was that a layer of nearly constant Richardson number existed in the entrainment zone of CBLs where shear made a sufficiently strong contribution to entrainment, we would expect profiles of Ri to exhibit such a layer in this case. The gradient (Ri_g) and flux (Ri_f) Richardson numbers were calculated as in Conzemius and Fedorovich (2006a), and their profiles in Fig. 9 are consistent with this described behavior. During the earliest stages of the simulation (Fig. 9a), the Ri profiles actually resemble that of the nocturnal PBL (Garratt 1992), with values approaching zero near the surface and increasing away from the surface. The value of 0.25 is not reached until $z = 400$ m. This early profile can be considered indicative of the transition from nocturnal to convective PBL in the presence of shear.

During the middle of the simulation (Fig. 9b), the layer of constant Ri is not quite so prevalent as in ear-

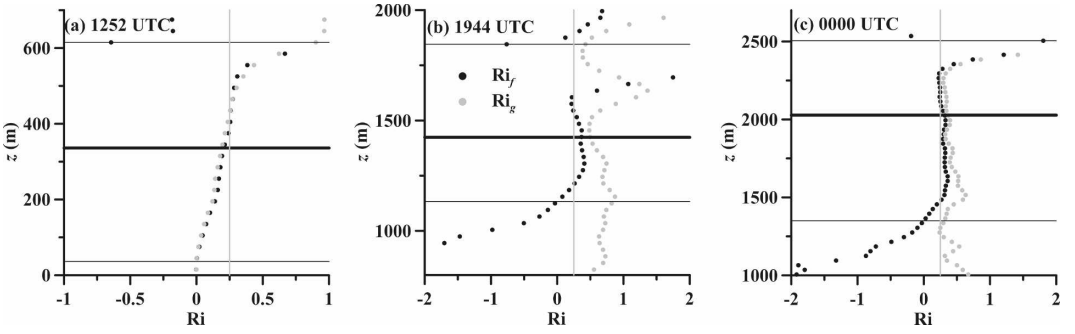

FIG. 9. Entrainment zone profiles of Ri_f (black circles) and Ri_g (gray circles) at (a) 1252, (b) 1944, and (c) 0000 UTC. The thick horizontal line indicates the CBL depth as determined from the buoyancy flux profile, and the thin horizontal lines indicate the lower and upper limits of the entrainment zone as defined by the vertical extent of the negative buoyancy flux (the upper limit is defined by the level where the buoyancy flux reaches 10% of its minimum at $z = z_i$).

lier and later stages in the simulation. Nevertheless, there is a shallow layer near $z = z_i$ where both Ri_g and Ri_f both drop to 0.5 or below.

At the end of the simulation (Fig. 9c), the layer of constant Ri is quite well established. Because the entrainment zone is well separated from the surface layer at this time, as well as between 1500 UTC and 1800 UTC (not shown), the constant Ri layer stands out as a separate entity. In all cases, the flux Richardson number Ri_f remains closer to the value of 0.25 than does Ri_g.

e. CBL depth compared to observations

The CBL depths determined from HARLIE data are compared with the simulated CBL depth evolution in Fig. 10. The lidar-determined CBL depths are missing during the early portion of the simulation because the lidar backscatter profile typically does not exhibit a sharp decrease in backscatter at the CBL top until later in the day when the CBL mixing is stronger and intensifies gradients in scatterers at the CBL top. In the simulation, the CBL undergoes a rather steady growth against the changing free atmospheric conditions. At first, the CBL growth is aided by shear but constrained by the strong stability. As shear decreases, the buoyancy flux increases, allowing the CBL growth to maintain a nearly constant rate. Near the end of the simulation, as surface buoyancy flux diminishes, the shear becomes strong and the stratification becomes weaker, allowing the CBL to continue growing steadily. All of these changes in forcing for CBL development cause its growth to deviate substantially from the $t^{1/2}$ relationship described for shear-free CBLs growing in constant stratification (Fedorovich et al. 2004a). See Fedorovich et al. (2004b) for a discussion on the effects of heterogeneous stratification on entrainment.

As can be expected, the wavelet-determined CBL depths in the simulation are a bit larger than those determined from the minimum of buoyancy flux. The simulated CBL depths agree with the HARLIE CBL depths most closely between 1630 and 1900 UTC. Thereafter, the lidar-determined CBL depths increase rapidly, whereas the simulated CBL depth maintains its original rate of growth. Even during the period of relative agreement, the lidar-determined CBL growth rate is somewhat faster than the simulated growth rate, and

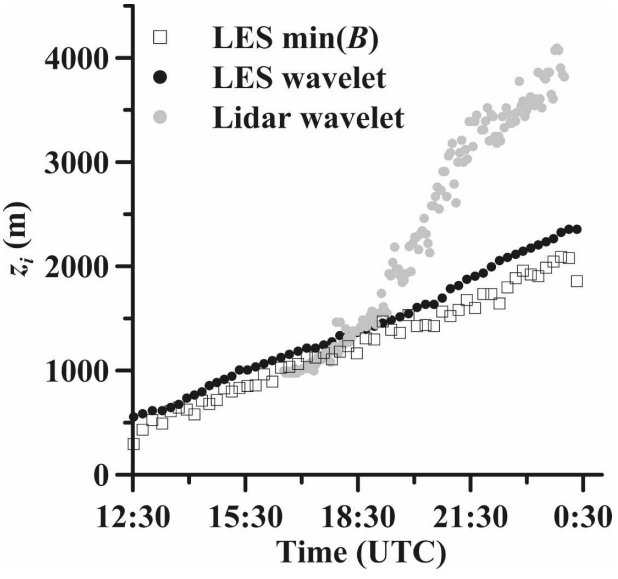

FIG. 10. The CBL depth z_i as a function of time for the 22 May 2002 simulation and concurrent lidar (HARLIE) data. The open squares denote the CBL depth as diagnosed from the minimum of buoyancy flux. The solid circles show the CBL depth values from the Haar wavelet transform on the vertical profiles of LES horizontally averaged virtual potential temperature (black circles) and lidar backscatter (gray circles).

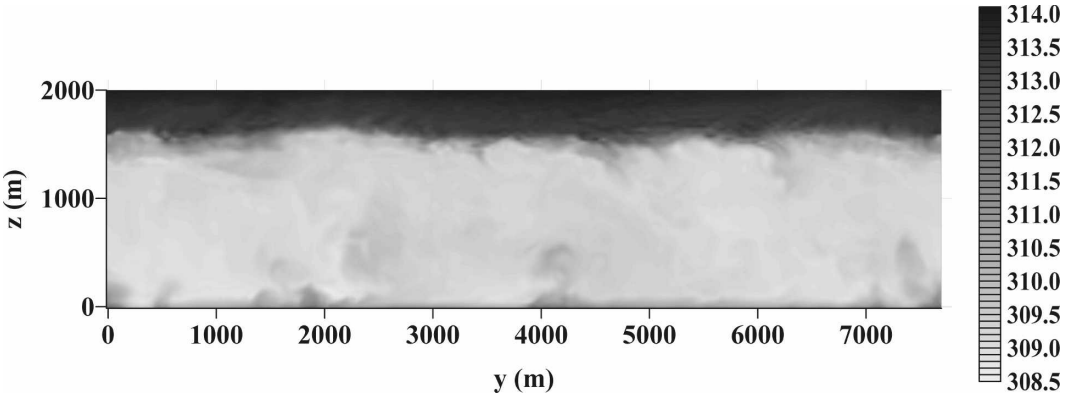

FIG. 11. The y–z cross section of instantaneous potential temperature (K) field at 1950 UTC (26 370 s into the simulation).

this difference increases rapidly after 1900 UTC. During the considered interval between 1900 and 2130 UTC, the lidar-determined CBL depth increases nearly 1800 m while the simulated depth increase is about one-fourth that amount (just over 400 m).

A look at the 1944 UTC ISS sounding in Fig. 6 reveals that the potential temperature gradient at the lidar wavelet-diagnosed CBL top (z = 1952 m) is about the same strength as the inversion above the CBL at the start of the simulation (with the caveat that the sounding cannot be horizontally averaged like the LES profiles are), yet it is about 200 m higher. The virtual potential temperature in the ISS sounding is also greater than in the simulations. Looking back at Fig. 3, one can see that the AERI potential temperature, which was used to initialize LES, is somewhat lower than the temperature provided by surface observations, but this difference is apparently too small to account for the differences in Fig. 6. On the other hand, data presented in Weiss et al. (2006) and Demoz et al. (2006) indicate that the dryline, which was located between the Homestead and S-Pol sites in the middle to late afternoon, had a large influence on the CBL structure.

As expected, the lidar-derived CBL depth estimates show large scatter associated with a smaller sampling area than the horizontally averaged area in LES. However, some of the scatter may also be due to the dryline proximity and the mixing that occurs at the CBL top at the dryline interface.

The LES technique is not well suited for the type of CBL heterogeneity occurring in this case. In particular, the code does not reproduce the features of the dryline (Ziegler and Hane 1993; Demoz et al. 2006; Weiss et al. 2006). It also does not account for the mechanisms responsible for this heterogeneity, such as variations in the land surface elevation, general west–east gradients in heat flux, and potential temperature advection, all of which may cause significant horizontal variations in CBL structure. The primary difficulty in using the LES technique for heterogeneous CBL is the necessity of using lateral boundary conditions for CBL-scale turbulence. Even if heterogeneous lower boundary conditions such as varying surface fluxes (see, e.g., Cai 1999) are applied or terrain is added (a general west-to-east slope as at the study site), the effects of accounting for these types of heterogeneity are eliminated when periodic boundary conditions are applied.

f. Simulated turbulence structure compared to observations

In this section, a y–z cross section, showing the turbulence structure from the simulations, is compared to a time–height cross section from the frequency-modulated, continuous-wave (FM-CW) S-band radar, which was located next to HARLIE in the IHOP_2002 experiment. Figure 11 shows the y–z cross section at 1950 UTC. The temperature field structure at the CBL top in Fig. 11 does show some evidence of the effects of shear in that the overshooting thermal elements tilt to the left, which is indicative of the negative shear in the y component of velocity in the entrainment zone. These structures resemble those displayed in Fig. 8 of Kim et al. (2003), who examined the entrainment zone structure of sheared CBLs.

In Fig. 12, the time–height cross section of the signal-to-noise ratio from the FM-CW radar is displayed and compared to the same simulated potential temperature field that is displayed in Fig. 11. Assuming a mean motion of 20 m s^{-1} in the CBL (from LES data) and using the Taylor frozen turbulence hypothesis to relate spatial and temporal scales of motion, the time span of 1 h in Fig. 12b would correspond to a horizontal domain width of 72 km in Fig. 11. Likewise, the CBL domain

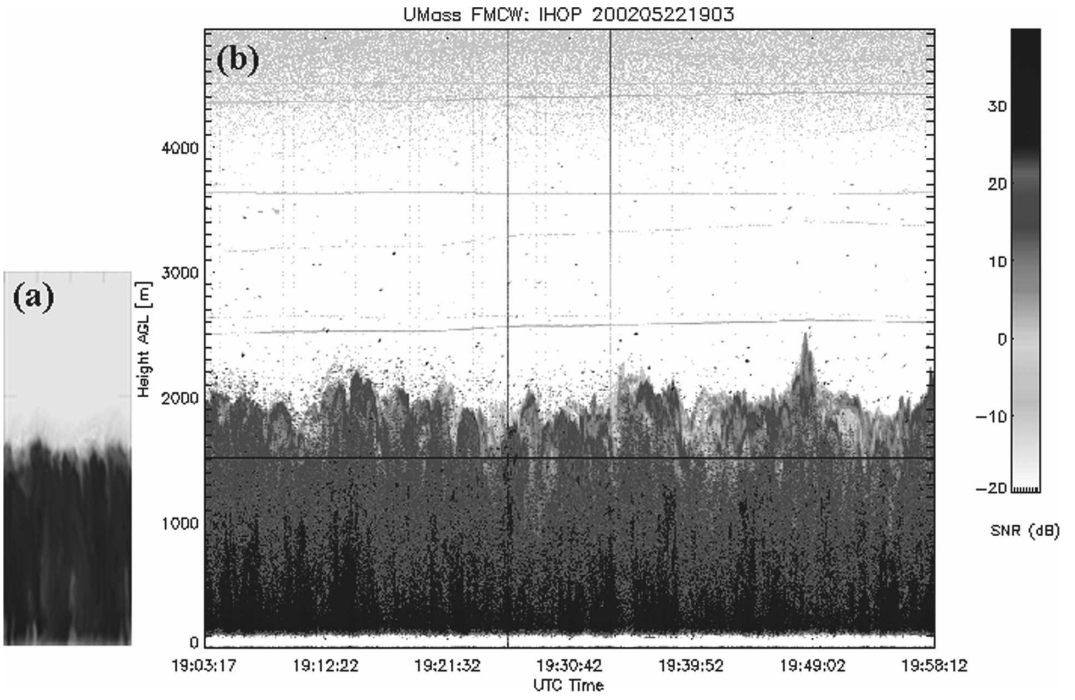

FIG. 12. CBL cross sections at concurrent times during the simulation and observations: (a) virtual potential temperature y–z cross section from the simulation at 1950 UTC (see Fig. 11), with its aspect ratio changed to match that of (b) the time–height cross section of signal to noise ratio (dB) from the University of Massachusetts FM-CW S-band radar from approximately 1900 to 2000 UTC.

in Fig. 11 corresponds to roughly the first 6 min of Fig. 12b.

The FM-CW cross section is taken from the overlapping time span of 1900–2000 UTC. At this point, the measured CBL depths were increasing rapidly because of the approach of the dryline. In the FM-CW data, the CBL top is marked by a large gradient in the signal-to-noise ratio, pointing to the sharp interface between the CBL air and the free-atmospheric air. The variability of the interface elevation in FM-CW is significantly larger than it is in LES. The increased variability in the FM-CW data is likely due to the effects of greater vertical velocity in the convective plumes as measured by Weiss et al. (2006) in the vicinity of the dryline as well as at the Homestead site (Demoz et al. 2006).

One particular feature to note is the variation of the sharpness of the CBL upper interface. When the tops of tall thermals penetrate into the free atmosphere, the local entrainment interface is sharper. In between, during times of prevailing downward motion, the interface is much less sharp and harder to define. This variable sharpness of the interface is generally seen in both the observed and simulated temperature structure patterns at the CBL top.

Finally, Fig. 13 shows the x–y cross section of potential temperature and horizontal wind fields at 1950 UTC from LES. The LES cross section highlights one particular issue in the comparison between measured structures from a stationary platform such as FM-CW and a vertical cross section from LES. In LES, the y–z cross section (see Fig. 11) is at an approximately 45° angle to the CBL flow and is therefore at an angle with respect to the horizontal convective rolls. Because the mean flow is typically aligned with the roll axis (Weckwerth et al. 1999), the cross-roll sampling of a stationary platform is relatively small and would best be mimicked by an LES vertical cross section that is aligned with the rolls. Lothon et al. (2006) describe the implications of cross-roll and along-roll sampling and their effects on measured vertical fluxes in the CBL.

Moeng and Sullivan (1994) found that roll structures are present when the negative of the ratio of the CBL depth to the Monin–Obukhov length is $-z_i/L < 2$ and that quasi-hexagonal cells dominate when $-z_i/L \gg 2$, with the Monin–Obukhov length defined as $L = -u_*^3/(\kappa B_s)$, where κ is the von Kármán constant, u_* is the surface friction velocity, and B_s is the surface buoyancy flux. Later, Weckwerth et al. (1999) found rolls to be possible for $-z_i/L < 25$. For the simulated CBL at 1950 UTC, $-z_i/L = \kappa w_*^3/u_*^3 = 11$ [where w_*^3 is the cube of the Deadorff (1970) convective velocity scale defined by $w_*^3 = B_s z_i$], which is within the range of cellular

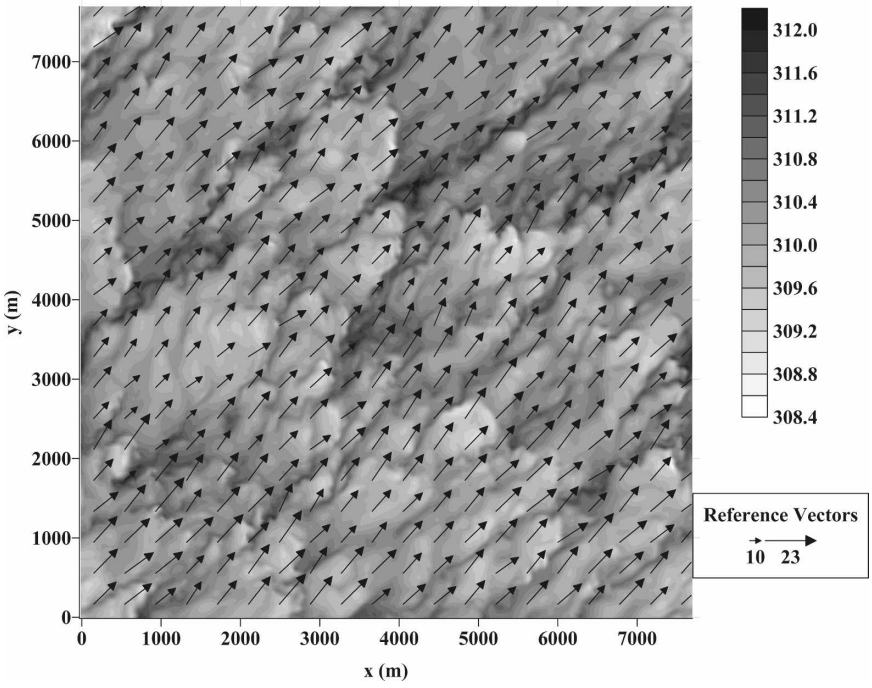

FIG. 13. The x–y cross section at 15 m above the surface showing potential temperature (K) and horizontal wind vectors (m s^{-1}) at 1950 UTC in the simulation.

convection indicated by Moeng and Sullivan (1994) but also within the range indicated by Weckwerth et al. (1999), where roll-like structures are possible. The ratio $-z_i/L$ varies from 0.5 at the beginning of the simulation, when the heat flux is weak and the CBL depth is small, to 11 in the middle, when the heat flux is strong and the CBL depth is large.

Given the variations of $-z_i/L$ during the simulation, one should expect the CBL turbulence structure to change. Indeed, at the beginning, the coherent features in the simulated CBL flow (not shown) appear more like the streaks that were observed by Khanna and Brasseur (1998) in a simulated shear-dominated boundary layer flow. The streaks then evolve into horizontal convective rolls, which, with further increasing $-z_i/L$, become less elongated and start to look somewhat more cell-like. Indeed, the structures in Fig. 13 appear to be in a hybrid state between rolls and cells but have a somewhat more cellular appearance. A complete transition to cellular structures never occurs in our simulation.

Figure 13 shows that in the surface layer of the simulated CBL, at 0026 UTC, the wind vectors are roughly parallel to the convective rolls. The strongest wind speeds are associated with the cooler air regions that have descended from the middle of the CBL (lighter gray shading in Fig. 13), and the weakest winds are generally found in the narrower plumes of warmer air, which are rising from the surface and carrying near-surface heat and momentum with them.

g. *Analysis of discrepancies between simulation and observations*

The three most significant discrepancies noted between LES and observations in the previous sections are the following:

1) the CBL depth is larger in the measurements than in LES (Figs. 6, 10, and 12);
2) the CBL potential temperature in the ISS 1944 UTC sounding is approximately 1 K warmer than the simulation (Fig. 6); and
3) the wind direction in LES is not representative of the winds in the reference location at the same time in the day on 22 May 2002, where the winds had a much smaller x component, coming from a direction of about 190° (Figs. 7 and 13).

The discrepancy in CBL depth can be explained by the approach of the dryline. Demoz et al. (2006) studied the dryline structure for this case in great detail and clearly show in their Fig. 2 that the dryline advanced eastward to a point between S-Pol and the Homestead site. Weiss et al. (2006) have convincingly demonstrated the presence of a solenoidal circulation associated with the west–east differences in density across the 22 May 2002 dryline. The upward branch of the circulation is

found just to the east of the dryline location and would have been over the Homestead site between 1900 and 2130 UTC. According to Demoz et al. (2006), the dryline at 2200 UTC was essentially collocated with the Homestead site and then retreated slowly westward. While the surface data at Homestead do not show a very large drop in water vapor typical of a dryline passage, the lidar-measured water vapor mixing ratios in the lowest 1 km of the atmosphere over the Homestead site dropped from 8–9 g kg^{-1} to 6–7 g kg^{-1} between 2130 and 2230 UTC.

The Weiss et al. (2006) dryline transects indicated a maximum updraft value of 8 m s^{-1}. If one were to perform a line average, parallel to the dryline and along the ascending branch of the solenoidal circulation, the mean vertical velocity would be considerably less than 8 m s^{-1} but would almost certainly be more than sufficient to account for the difference between the simulated and observed CBL growth between 1830 and 2130 UTC. A mean vertical velocity of 0.14 m s^{-1} at the CBL top is all that is needed in this case. The data in Weiss et al. (2006) clearly suggest that the solenoidal circulation is greater than this magnitude. One may conclude that the dryline proximity and the vertical motion are sufficient to explain the difference between the CBL depth measured locally at Homestead and the simulated CBL depth.

One possible explanation for the discrepancy in CBL potential temperature is the large-scale temperature advection, which was neglected in the simulation. A calculation of potential temperature advection using the RUC analysis on a grid with an isobaric vertical coordinate did not support this hypothesis. In general, the differential advection (cold in the CBL and warm above the CBL) would have slowed boundary layer growth east of the dryline and sped the growth west of the dryline. We suspect that the RUC grid is too coarse to properly resolve the dryline structure in the vicinity of the Homestead site and is therefore unable to provide a sufficiently accurate estimate of local advection to explain the relatively small difference in simulated versus observed virtual potential temperature.

After looking at the differences in the large-scale pressure gradient and the Coriolis forces in RUC and LES, the reasons for the discrepancies between the observed and simulated winds become clear. Figure 14 shows time series of x and y components of acceleration associated with these forces in the lowest 125-mb layer above the study site. Although the large-scale pressure gradient varied relatively little during the course of the day, the absolute value of the change was enough to significantly affect the simulated wind. A 0.000 25 m s^{-2} acceleration is enough to cause a 0.9 m s^{-1} change in wind velocity over 1 h. For the u component of the wind, the additional acceleration in LES over RUC is approximately equal to or larger than this value over the first several hours of the simulation, so a difference of several meters per second can be expected. For the v component, the differences are even larger, and they are in a direction that can explain the differences between LES and RUC. For a more rigorous numerical investigation of the time evolution of the mean flow, the geostrophic wind components should be allowed to change with time. The large-scale advection should also be taken into account, although its effect in the considered CBL case was relatively weak. Alternatively, a larger surface roughness length could be prescribed in LES (to allow more cross-isobaric flow toward low pressure to the north), but the employed value of 0.01 m is believed to be representative of the conditions in the Oklahoma and Texas Panhandles.

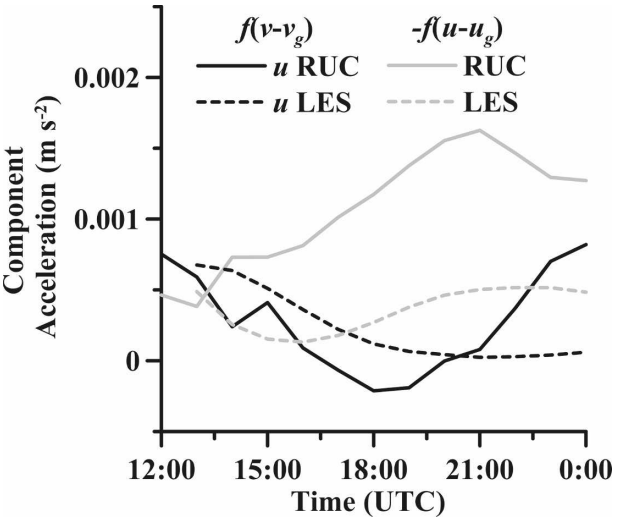

FIG. 14. Time series of u and v velocity component accelerations resulting from the large-scale pressure gradient and Coriolis forces in RUC and LES. The black lines denote the u component and gray lines the v component. The solid lines represent RUC data, and the dashed lines are derived from LES.

4. Discussion and conclusions

The results of the simulations and comparison with observations can be summarized with respect to the original goals of the study. Simulations based on 22 May 2002 data have demonstrated that the shear enhancement of entrainment in the realistic CBL can be equal to or greater than that in the idealized simulations initiated with linear temperature and velocity profiles, as in Conzemius and Fedorovich (2006a). In es-

sence, the results of that earlier study were confirmed in the present comparison. The simulated CBL depths match the lidar-determined CBL depths relatively closely between 1530 and 1900 UTC, which is an indication that, at least for the first portion of the simulation, LES is able to faithfully reproduce the CBL evolution.

In particular, the results of the present study are consistent with the two following findings of our earlier study: (i) a layer of constant Ri is found in the entrainment zone of sheared CBLs where the shear is sufficiently strong, and its value is approximately 0.25; and (ii) the surface layer shear does not contribute directly to the TKE available for entrainment. The first finding is confirmed by layers of nearly constant Ri in the entrainment zone in the simulated 22 May 2002 case, which are relatively deep both early and late in the simulation, when the shear is strongest, and shallower in the middle of the simulation, when the entrainment zone shear is weakest. The second finding is also supported by the 22 May 2002 simulation results. In the middle of the simulation, the surface shear remains strong, yet the entrainment flux ratio drops closer to 0.2. Such behavior is similar to nearly shear-free CBLs, and the fact that the entrainment zone shear is somewhat weaker during the middle of the simulation, while the surface layer shear remains strong, indicates that it is the entrainment zone shear that is providing the majority of the shear-generated TKE that is used for entrainment.

There are, however, some significant differences between the simulation and the observations. Between 1900 and 2130 UTC, the CBL depth increases much more rapidly in the observations than it does in the simulations. This difference in depth can be explained by the approach of the dryline at the Homestead site, which has been well documented in previous studies of the 22 May 2002 dryline. The heterogeneity of the CBL structure along a dryline cannot be represented faithfully under the constraints of periodic boundary conditions in LES.

The difference in wind direction between the simulations and the observations deserves special consideration. Analyses of the Coriolis and large-scale pressure gradient forces showed that their evolutions were quite different between the RUC predictions and LES for this case. The magnitudes of these differences are sufficient to explain the discrepancies in the wind vector. We find, therefore, that the time variation of the large-scale pressure gradient, which was neglected in LES, is a necessary factor to be considered. The large-scale (external with respect to the LES domain) advection of momentum should probably be considered as well. Additionally, the 1944 UTC sounding from ISS shows greater virtual potential temperature over the depth of the CBL than does the simulation, but the available RUC data were not able to sufficiently resolve the dryline structure near the site to explain the relatively small discrepancy in virtual potential temperature.

Patterns of the CBL flow structure can be readily compared between observations and simulations for this case, although these comparisons are mostly qualitative, with the differences in wind direction and CBL depth making quantitative comparisons rather difficult. More insight into the ability of LES to faithfully reproduce CBL turbulence structures could be gained by analyzing turbulence velocity spectra. Such an analysis would require the development of a postprocessing procedure to bring the observational data into a suitable framework of comparison with the simulations. For example, one might process mobile radar data onto a Cartesian grid to allow for a direct comparison with LES and then filter the LES data so that their grid interval can optimally match the range gate of a radar platform. Aircraft data could also be utilized for this purpose and should also be considered. Such techniques, however, would deserve the attention of a fully separate study.

Despite these concerns, the simulated evolution of the entrainment process was rather indicative of how it occurs in the atmosphere. During the early stages of the simulation, shear enhancement of entrainment was fairly large. During the middle stages, shear had little influence on entrainment, but by the end, the effects of shear were becoming important again. This cycle of shear effects somehow mirrors the change in surface buoyancy flux, which allows the relative effect of shear to be more protuberant early and late in the simulation. The changes of shear in the entrainment zone reflect the combined impact of surface buoyancy forcing and bulk shear: the shear is strong early in the simulation, weak in the middle, and again stronger at the end. When the shear is strong, its effects are clearly seen in the entrainment zone depth, the entrainment flux ratio, the TKE budgets, and the Richardson number profiles.

Future work related to this study will involve improvements to the LES code to incorporate the time evolution of large-scale pressure gradient forces as well as the effects of advection. It may be additionally possible to modify the LES code so that it can be used to simulate heterogeneous CBLs using larger LES domains and more flexible boundary conditions. If the two interacting CBL types associated with a dryline could be simulated simultaneously, the simulation

might elucidate the dynamics that drive dryline processes. It appears to be a challenging topic for future research.

Acknowledgments. This work has been supported by National Science Foundation Grant ATM-0124068. The first author would like to thank members of his Ph.D. advisory committee Charles A. Doswell III, Brian Fiedler, Randall Kolar, Douglas Lilly, and Alan Shapiro for their insightful comments on this study.

REFERENCES

Angevine, W. M., A. W. Grimsdell, S. A. McKeen, and J. M. Warnock, 1998: Entrainment results from the Flatland boundary layer experiments. *J. Geophys. Res.,* **103,** 13 689–13 701.

——, H. K. Baltink, and F. C. Bosveld, 2001: Observations of the morning transition of the convective boundary layer. *Bound.-Layer Meteor.,* **101,** 209–227.

Cai, X. M., 1999: Large-eddy simulation of the convective boundary layer over an idealized patchy urban surface. *Quart. J. Roy. Meteor. Soc.,* **125,** 1427–1444.

Conzemius, R. J., 2004: The effects of wind shear on the convective boundary layer entrainment. Ph.D. dissertation, University of Oklahoma, 338 pp.

——, and E. Fedorovich, 2006a: Dynamics of sheared convective boundary layer entrainment. Part I: Methodological background and large-eddy simulations. *J. Atmos. Sci.,* **63,** 1151–1178.

——, and ——, 2006b: Dynamics of sheared convective boundary layer entrainment. Part II: Evaluation of bulk model predictions of entrainment flux. *J. Atmos. Sci.,* **63,** 1179–1199.

——, and ——, 2007: Bulk models of the sheared convective boundary layer: Evaluation through large eddy simulations. *J. Atmos. Sci.,* **64,** 786–807.

Davis, K. J., N. Gamage, C. R. Hagelberg, C. Kiemle, D. H. Lenschow, and P. P. Sullivan, 2000: An objective method for deriving atmospheric structure from airborne lidar observations. *J. Atmos. Oceanic Technol.,* **17,** 1455–1468.

Deardorff, J. W., 1970: Convective velocity and temperature scales for the unstable planetary boundary layer and for Raleigh convection. *J. Atmos. Sci.,* **27,** 1211–1213.

——, 1980: Stratocumulus-capped mixed layers derived from a three dimensional model. *Bound.-Layer Meteor.,* **18,** 495–527.

Demoz, B., and Coauthors, 2006: The dryline on 22 May 2002 during IHOP_2002: Convective-scale measurements at the profiling site. *Mon. Wea. Rev.,* **134,** 294–310.

Fedorovich, E., F. T. M. Nieuwstadt, and R. Kaiser, 2001: Numerical and laboratory study of a horizontally evolving convective boundary layer. Part I: Transition regimes and development of the mixed layer. *J. Atmos. Sci.,* **58,** 70–86.

——, R. Conzemius, and D. Mironov, 2004a: Convective entrainment into a shear-free, linearly stratified atmosphere: Bulk models reevaluated through large eddy simulations. *J. Atmos. Sci.,* **61,** 281–295.

——, ——, and A. Shapiro, 2004b: Nonstationarity of convective boundary layer growth in a heterogeneously stratified, shear-free atmosphere. Preprints, *16th Symp. on Boundary Layers and Turbulence,* Portland, ME, Amer. Meteor. Soc., 7.9. [Available online at http://ams.confex.com/ams/pdfpapers/78683.pdf.]

——, and Coauthors, 2004c: Entrainment into sheared convective boundary layers as predicted by different large-eddy simulation codes. Preprints, *16th Symp. on Boundary Layers and Turbulence,* Portland, ME, Amer. Meteor. Soc., P4.7. [Available online at http://ams.confex.com/ams/pdfpapers/78656.pdf.]

Feltz, W. F., W. L. Smith, H. B. Howell, R. O. Knuteson, H. Woolf, and H. E. Revercomb, 2003: Near continuous profiling of temperature, moisture, and atmospheric stability using the Atmospheric Emitted Radiance Interferometer (AERI). *J. Appl. Meteor.,* **42,** 584–597.

Garratt, J. R., 1992: *The Atmospheric Boundary Layer.* Cambridge University Press, 316 pp.

Guerra, D., G. Schwemmer, A. Wooten, S. Chaudhuri, and T. Wilkerson, 1999: Prototype holographic atmospheric scanner for environmental remote sensing. *J. Geophys. Res.,* **104D,** 22 287–22 292.

Holtslag, A. A. M., and P. G. Duynkerke, Eds., 1998: *Clear and Cloudy Boundary Layers*. Royal Netherlands Academy of Arts and Sciences, 372 pp.

Khanna, S., and J. G. Brasseur, 1998: Three-dimensional buoyancy- and shear-induced local structure of the atmospheric boundary layer. *J. Atmos. Sci.,* **55,** 710–743.

Kim, S.-W., S.-U. Park, and C.-H. Moeng, 2003: Entrainment processes in the convective boundary layer with varying wind shear. *Bound.-Layer Meteor.,* **108,** 221–245.

Lenschow, D. H., 1970: Airplane measurements of planetary boundary layer structure. *J. Appl. Meteor.,* **9,** 874–884.

——, 1974: Model of the height variation of the turbulence kinetic energy budget in the unstable planetary boundary layer. *J. Atmos. Sci.,* **31,** 465–474.

Lothon, M., D. H. Lenschow, and S. Mayor, 2006: Coherence and scale of vertical velocity in the convective boundary-layer from a Doppler lidar. *Bound.-Layer Meteor.,* **121,** 521–536.

Moeng, C.-H., and P. P. Sullivan, 1994: A comparison of shear- and buoyancy-driven planetary boundary layer flows. *J. Atmos. Sci.,* **51,** 999–1022.

Nieuwstadt, F. T. M., and R. A. Brost, 1986: The decay of convective turbulence. *J. Atmos. Sci.,* **43,** 532–546.

Peckham, S. E., R. B. Wilhelmson, L. J. Wicker, and C. L. Ziegler, 2004: Numerical simulation of the interaction between the dryline and horizontal convective rolls. *Mon. Wea. Rev.,* **132,** 1792–1812.

Pino, D., J. V.-G. de Arellano, and P. J. Duynkerke, 2003: The contribution of shear to the evolution of a convective boundary layer. *J. Atmos. Sci.,* **60,** 1913–1926.

Stull, R. B., 1973: Inversion rise model based on penetrative convection. *J. Atmos. Sci.,* **30,** 1092–1099.

Sullivan, P., C.-H. Moeng, B. Stevens, D. H. Lenschow, and S. D. Mayor, 1998: Structure of the entrainment zone capping the convective atmospheric boundary layer. *J. Atmos. Sci.,* **55,** 3042–3064.

Weckwerth, T. M., T. W. Horst, and J. W. Wilson, 1999: An observational study of the evolution of horizontal convective rolls. *Mon. Wea. Rev.,* **127,** 2160–2179.

——, and Coauthors, 2004: An overview of the International H_2O Project (IHOP_2002) and some preliminary highlights. *Bull. Amer. Meteor. Soc.,* **85,** 253–277.

Weiss, C. C., H. B. Bluestein, and A. L. Pazmany, 2006: Finescale radar observations of the 22 May 2002 dryline during the International H_2O Project (IHOP). *Mon. Wea. Rev.,* **134,** 273–293.

——, ——, R. Conzemius, and E. Fedorovich, 2007: Variational

pseudo-multiple-Doppler wind retrieval in the vertical plane for ground-based mobile radar data. *J. Atmos. Oceanic Technol.,* **24,** 1165–1185.

Xue, M., and W. J. Martin, 2006a: A high-resolution modeling study of the 24 May 2002 dryline case during IHOP. Part I: Numerical simulation and general evolution of the dryline and convection. *Mon. Wea. Rev.,* **134,** 149–171.

——, and ——, 2006b: A high-resolution modeling study of the 24 May 2002 dryline case during IHOP. Part II: Horizontal convective rolls and convective initiation. *Mon. Wea. Rev.,* **134,** 172–191.

Ziegler, C. L., and C. E. Hane, 1993: An observational study of the dryline. *Mon. Wea. Rev.,* **121,** 1134–1151.

——, T. J. Lee, and R. A. Pielke Sr., 1997: Convective initiation at the dryline: A modeling study. *Mon. Wea. Rev.,* **125,** 1001–1026.